Surv Geophys (2016) 37:791–809
DOI 10.1007/s10712-015-9355-x

Worst-Case GPS Scintillations on the Ground Estimated from Radio Occultation Observations of FORMOSAT-3/COSMIC During 2007–2014

J. Y. Liu[1] · S. P. Chen[1] · W. H. Yeh[2] · H. F. Tsai[3] · P. K. Rajesh[3]

Received: 13 August 2015 / Accepted: 14 December 2015 / Published online: 4 January 2016

Abstract The FORMOSAT-3/COSMIC (F3/C) satellite probes the S4 scintillation index profile of GPS signals by using the radio occultation (RO) technique. In this study, for practical use on the Earth's surface, a method is developed to convert and integrate the probed RO S4 index, so obtaining the scintillation on the ground. To estimate the worst case, the maximum value on each profile probed by F3/C, which is termed S4max, is isolated. The isolated data are further used to construct the global three-dimensional distributions of S4max for various local times, seasons, solar activities, and locations. The converted S4max for the first time estimates the global distribution of ionospheric scintillations in the GPS L1 band C/A code signal on the ground. The results show that the worst-case scintillations appear within the low-latitude region of ±30°N, peaking around ±20°N magnetic latitude; they begin at 1900 MLT, reach their maximum at 2100 MLT, and vanish by about 0200–0300 MLT. The most pronounced low-latitude scintillation occurs over the South American and African sectors.

Keywords FORMOSAT-3/COSMIC satellite · Radio occultation · Ionospheric scintillation · S4 index

1 Introduction

Scintillation can be defined formally as a random modulation imported onto propagating wave fields by structures in the propagation medium (Rino 2011). Thus, scintillation observations have been employed to identify and diagnose irregular structures in highly

✉ J. Y. Liu
tigerjyliu@gmail.com

[1] Institute of Space Science, National Central University, Taoyuan, Taiwan

[2] GPS Science and Application Research Center, National Central University, Taoyuan, Taiwan

[3] Department of Earth Sciences, National Cheng Kung University, Tainan, Taiwan

varied propagation media. The research on scintillations started during the 1950s. Parthasarathy (1959) reported scintillations in the auroral region. Following that, Frihagen and Troim (1960) using 20 MHz signals from an Earth-orbiting satellite observed signal scintillations at solar maximum, and Hook and Owren (1962) derived the ionospheric E-region irregularity distribution from satellite radio signals (20.005 and 40 MHz).

Numerous studies have been conducted since then (Rastogi 1980; Aarons et al. 1983; Watanabe and Oya 1986; Basu et al. 1988; Sahai et al. 2000; Abdu 2001; Huang et al. 2002; Burke et al. 2004; Thampi et al. 2009). Basu et al. (1988) employed limited observations of ground-based radars (Huancayo, Ascension Island, Goose Bay, Tromsø, and Thule) and satellite beacons (1.54 GHz from the Marisat satellite, polar beacon satellites at 250, the 244 MHz signal from the Fleetsatcom satellite, and wide band satellite data at 137 MHz) to construct a map of L-band (1.54 GHz) scintillations for periods of different solar activity. However, the map lacked longitudinal information due to the radars mainly being located in the American sector. Recently, GPS amplitude and/or phase scintillations were observed on the ground (Aarons et al. 1997; Mendillo et al. 2000). More recently, Olwendo (2013) derived the S4 index of GPS signals at geomagnetic equatorial latitudes in 2011–2012. Although ground-based GPS receivers continuously monitor the S4 index, they lack coverage in ocean and remote areas.

With the advent of GPS, the technique of radio occultation (RO) has been developed in the 1990s. The technique of RO uses low Earth orbit (LEO) satellites at several hundred kilometers in altitude to receive the GPS signals. The RO observations can uniformly provide the global distribution of atmospheric and ionospheric parameters, such as air pressure, temperature, electron density, and scintillation with high vertical resolution (Scherliess and Fejer 1999; Yunck et al. 2000; Wickert et al. 2001), which significantly improves the coverage of the traditional ground-based observations. With the GPS receiver onboard a LEO satellite, the ionospheric irregularities were studied using the RO technique (Hocke et al. 1999; Sokolovskiy et al. 2002; Straus et al. 2003; Wu et al. 2005, 2006; Arras et al. 2008). By contrast, with a six-microsatellite constellation, Uma et al. (2012) and Brahmanandam et al. (2012) reported the global three-dimensional (3D) structure of S4max, the maximum value of each S4 profile recorded by F3/C (FORMOSAT-3/COSMIC). Although 3D S4max structures were investigated, for practical applications, the worst case on the ground, similar to that discussed by Basu et al. (1988), has not yet been developed and reported.

In this paper, a method is introduced which converts the space-based F3/C RO S4 index observations to the ground-based situation. To carry out the conversion, 3D structures of S4max are constructed, which allows us to understand GPS scintillation variations at various local times, seasons, and solar activity conditions, as well as the geographical distribution from the space-based point of view. By applying the method to data of the 3D structure, maps of the worst-case scenario on the ground as functions of geomagnetic local time and geographic coordinates are constructed and reported here.

2 F3/C Microsatellites and Data Conversion Method

The Formosa satellite 3, also named the Constellation Observing System for Meteorology, Ionosphere, and Climate (abbreviated as FORMOSAT-3/COSMIC, or F3/C for short), is a constellation of six microsatellites, designed to monitor weather and space weather with its major payload, a GPS radio occultation receiver developed by NASA's JPL (Jet Propulsion

Laboratory), performing the RO observations in both the atmosphere and the ionosphere (Anthes et al. 2008). Here, we examine the scintillation S4 index observations between GPS and F3/C satellites from the GPS RO payload. The mission orbits are around 800 km altitude, 72° inclination angle, and with a 30° separation in longitude between each microsatellite. The F3/C scintillation data are calculated as the S4 index by using the signal to noise ratio on the L1 band C/A code (1.575 GHz) [see Syndergaard (2006) at http://cdaac-www.cosmic.ucar.edu/cdaac/doc/documents/s4_description.pdf]. The signal to noise intensity fluctuations from the raw 50-Hz L1 amplitude measurements are computed, while these intensity measurements are recorded in the data stream at a 1-Hz rate. Due to the number of satellites, F3/C obtained up to 3000 scintillation profiles per day. The scintillation profiles are recorded in the scintillation files (data type scnLv1) and can be obtained from the Taiwan Analysis Center for COSMIC (TACC) and/or COSMIC Data Analysis and Archive Center (CDAAC). In scnLv1, the value, the longitude, latitude, and altitude of each S4max are recorded.

In order to convert the space-based F3/C RO scintillation to the ground-based one, a new method is developed. Figure 1 illustrates the conversion method, where P is the position of the tangent point of the straight line between GPS and LEO satellite, and L3 is the distance between P and the Earth's center. The length of L2, which is the layer thickness, is set to be 1 km. The L1 is the tangent line of the circle with the radius L3 and with the point of tangency P. The two end points of L1, P1 and P2, are with the distance L2 + L3 from the Earth's center. The conversion is performed under the following four assumptions. First, the electron density fluctuations on the signal propagating path in the shell, which has inner and outer radii L3 and L2 + L3, respectively, is the main source of the amplitude fluctuations. Secondly, the electron density fluctuations in the shell are uniform. Thirdly, in the uniform electron density fluctuations, the value of the S4 scintillation index is proportional to the signal propagating distance. Fourthly, the S4 scintillation index follows the superposition principle. Following these assumptions, the equation of the conversion can be written as

$$S_{4,\text{vertical}} = \frac{L2}{L1} S_{4,\text{horizontal}} \tag{1}$$

where $S_{4,\text{horizontal}}$ and $S_{4,\text{vertical}}$ are the values of the S4 index before and after the conversion, respectively. By using Eq. (1), the S4 index of the signal which propagates

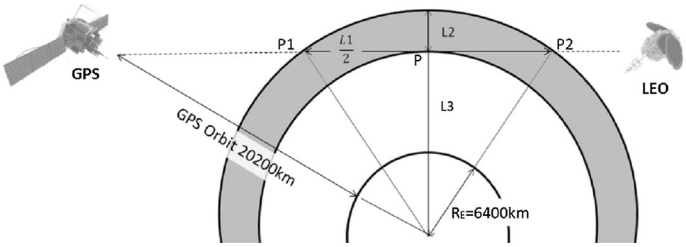

Fig. 1 Illustration of the conversion method to convert the space-based F3/C RO scintillation to the ground-based one. P denotes the position of the tangent point of the straight line between the GPS and LEO satellites, and L3 is the distance between P and the Earth's center. The length of L2, which is the layer thickness, is set to be 1 km. The L1 is the tangent line of the *circle* with the radius L3 and with the point of tangency P. The two end points P1 and P2 of L1 have the distance of L2 + L3 from the Earth's center

horizontally through the shell over the distance L1 can be converted to the S4 index of the signal which propagates vertically through the shell over the distance L2.

In order to gather the converted S4 index data, a matrix with 360 × 180 × 700 grids is used to indicate the geomagnetic local time (MLT), geomagnetic latitude (mLat), and altitude, respectively. The ranges of MLT, mLat, and altitude are 0–24 h, −90° to 90°, and 50–750 km, respectively, and therefore their resolutions are 4 min, 1 degree, and 1 km, respectively. With models of the International Geomagnetic Reference Field IGRF (Thébault et al. 2015) and modified dip latitude Modip (Azpilicueta et al. 2006), and the constructed matrix, we can interchange between MLT and geographic longitude (Lon) as well as between geographic latitude (Lat) and mLat. Based on the time, location, and altitude, each S4max will be put into its specified grid, and the median value of each grid computed accordingly. Equation (1) is further applied to vertically integrate S4max from 50 to 750 km altitude at the certain location, and construct a two dimensional MLT-mLat map, with 360 × 180 grids.

3 Observations and Results

The F3/C GPS RO observations are further subdivided into 4 seasons, M-month (±45 days to March equinox), J-month (±45 days to June solstice), S-month (±45 days to September equinox), and D-month (±45 days to December solstice). The 3D analysis on various MLTs, mLats, and altitudes during the 4 months of the two solar activity periods studied, which are the solar minimum of 2008–2010 and the solar maximum of 2012–2014, are investigated. Figure 2 shows S4max at 80–150 and 150–600 km altitude.

During the solar minimum, the equatorial scintillations become prominent from the post-sunset hours and often persist until the post-midnight hours (i.e., from 1800 to 0200 MLT) at the bottom side of the F-region, 150–350 km altitude (Fig. 2a). In general, the S4max intensity reaches its maximum within ±25°N mLat, at 200–250 km altitude, and at 2200–2300 MLT. The F-region S4max yields stronger intensities and expands to higher latitudes in M-, S-, and D-months. Further, the scintillation activity in the E-region (80–150 km altitude bin) is more prominent in both daytime (0900 MLT) and nighttime (1900 MLT), and appears in mid-latitudes (30°–40°N mLat) of both northern and southern hemispheres. Note that the E-region S4max reaches its maximum intensity in the summer hemisphere, i.e., J-month in the northern hemisphere and D-month in southern hemisphere, and the intensity in the northern hemisphere of J-month is stronger than that in the southern hemisphere of D-month.

The distribution and appearance time of the S4max during the solar maximum generally are similar to those during the solar minimum, except being of stronger intensity and expanding to higher, even up to 600 km, altitudes. Here, the F-region S4max yields stronger intensities and expands to higher latitudes/altitudes in M-, S-, and D-months. By contrast, the E-region S4 index during the solar maximum is very similar to that during the solar minimum which suggests that the solar activity effect is not essential in the E-region but is for the seasonal one.

Based on the proposed method, the observations shown in Fig. 2 are converted into the worst-case maps of MLT versus mLat observed on the ground in various seasons during the solar minimum and solar maximum. Figure 3 depicts that, during the solar minimum, the converted scintillation yields the greatest value in M-month, greater in D-month, smaller in S-month, and smallest in J-month. It can be seen that the scintillations have a

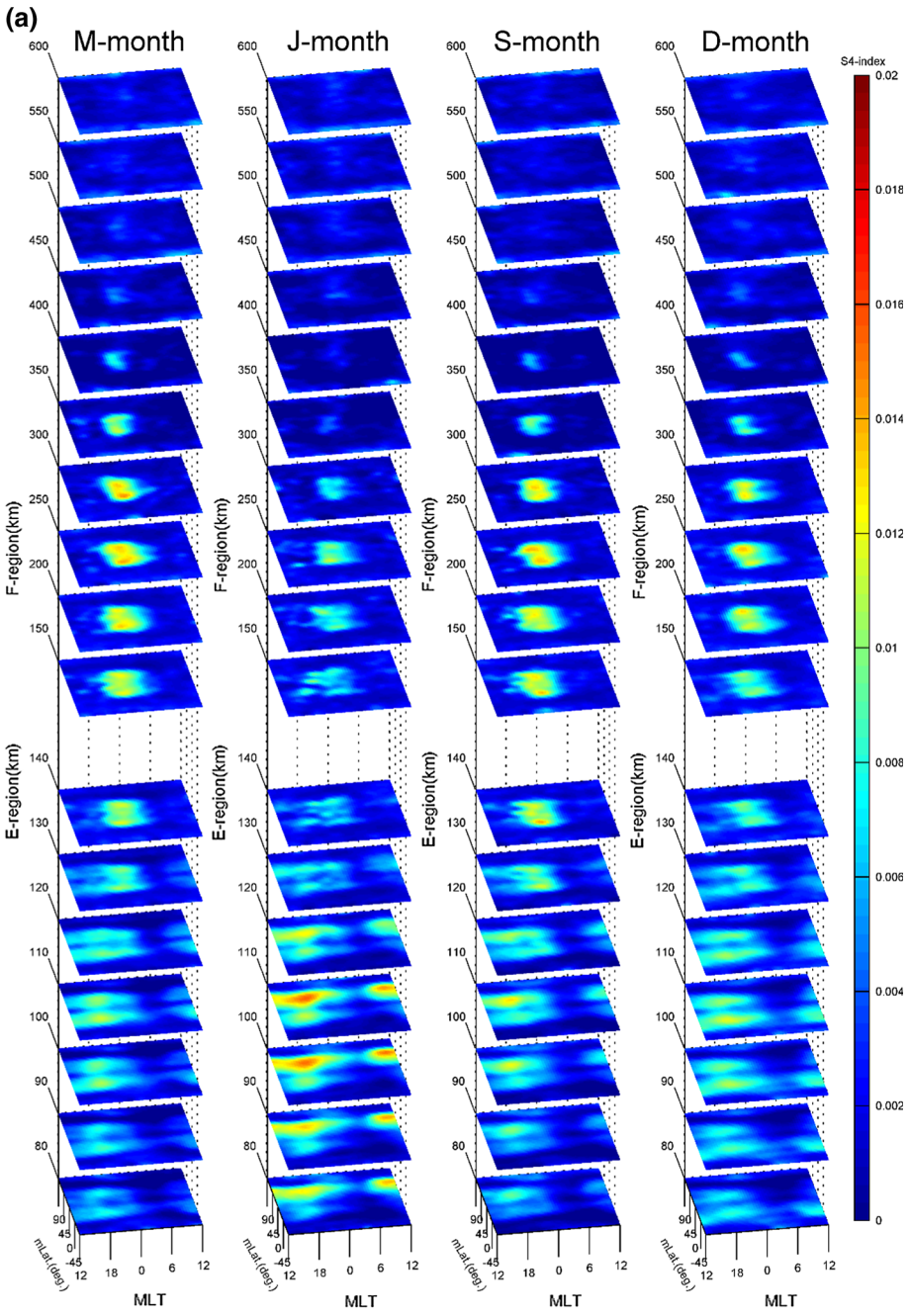

Fig. 2 S4max for magnetic latitude versus magnetic local time at 80–150 and 150–600 km altitude during the solar minimum (**a**) and solar maximum (**b**). Four columns from left to right stand for M-, J-, S-, and D-months, respectively. The altitude resolution is 10 m and 50 km in the E-region (80–150 km) and F-region (150–600 km), respectively

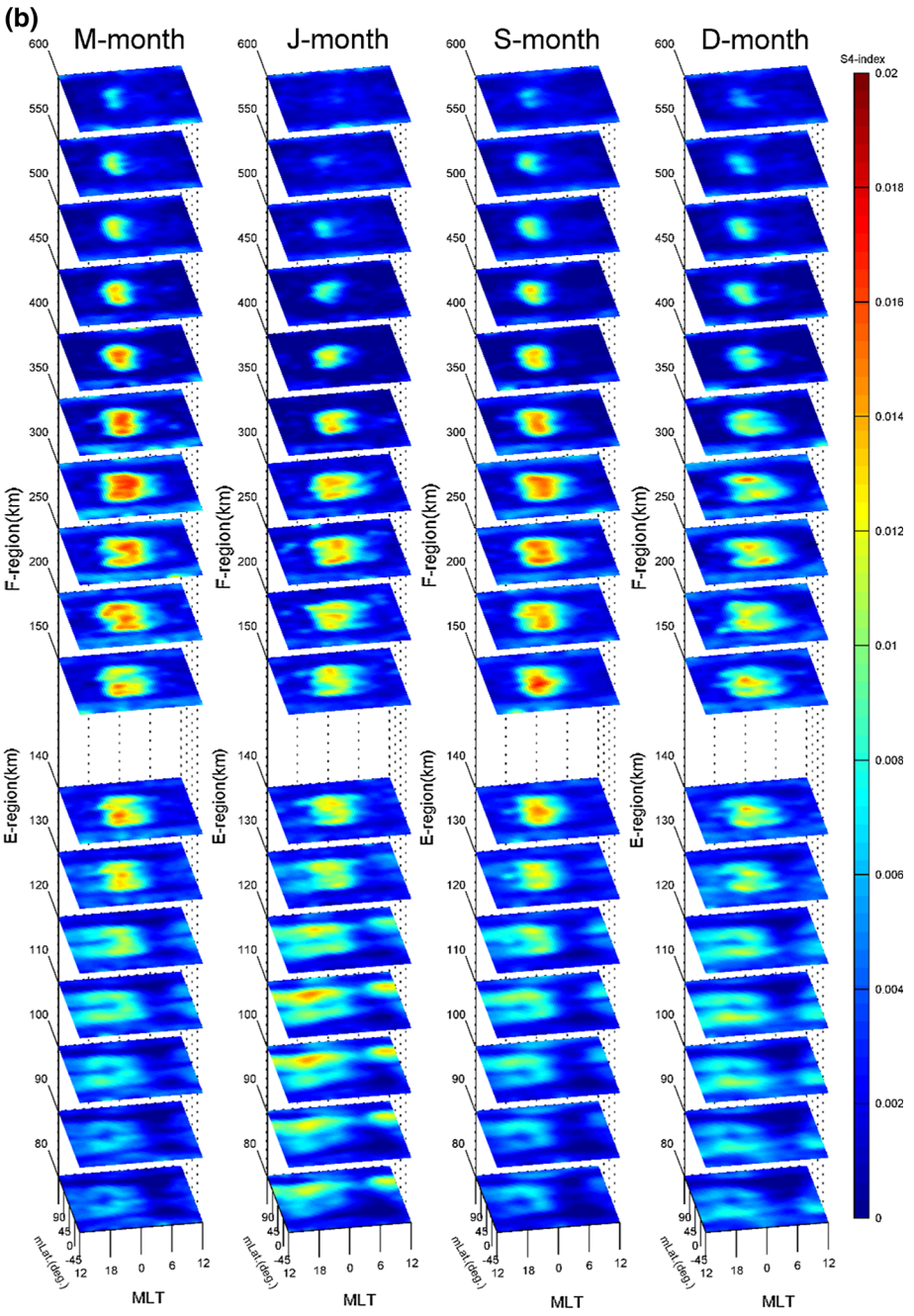

Fig. 2 continued

double-peaked feature, which settles on both sides of the magnetic equator and centers at about ±10°, is confined to low magnetic latitudes within ±30°, appears from 2000 MLT, enhances intensely at 2100 MLT, reaches the maximum at 2200–0100 MLT, and finally

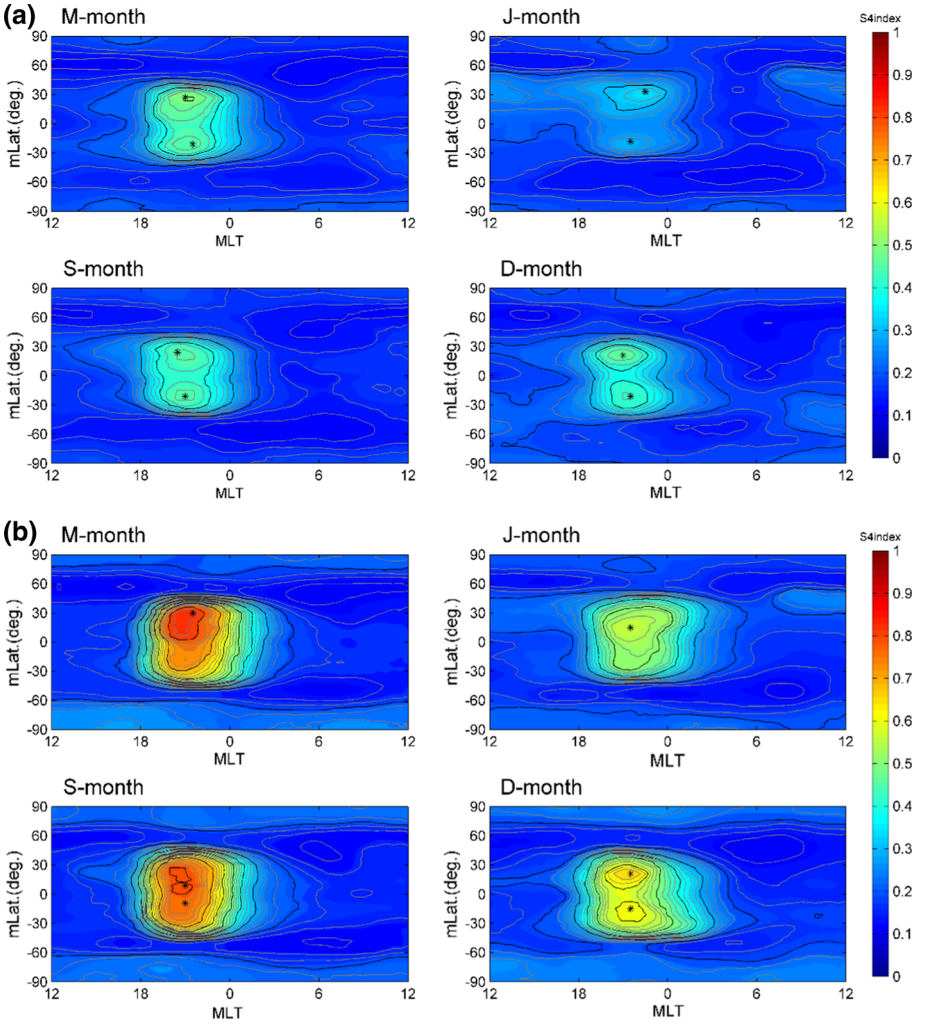

Fig. 3 The vertical integration of S4max from 50 to 750 km altitude in Fig. 2 during the solar minimum (**a**) and solar maximum (**b**). The *asterisk* symbols denote the peak of the S4max

dissipates after 0200 MLT. By contrast, during the solar maximum, scintillation yields the greatest value in S-month, greater in M-month, smaller in D-month, and smallest in J-month. Although daily evolutions are generally similar, the scintillation in each month during the solar maximum is greater than that of the solar minimum, accordingly. It can be seen that the clear double-peaked structure appears in the 4 months during both solar minimum and maximum. Figure 3 further reveals that the low-latitude scintillation expands to higher latitudes, and the polar-latitude scintillation becomes intense during the solar maximum.

To compare our results with those of Basu et al. (1988), we superimpose the maps of the 4 months shown in Fig. 3 and apply the Hammer projection (MATLAB R2010a) obtaining the worst-case maps during the solar minimum and maximum. Since in this study the

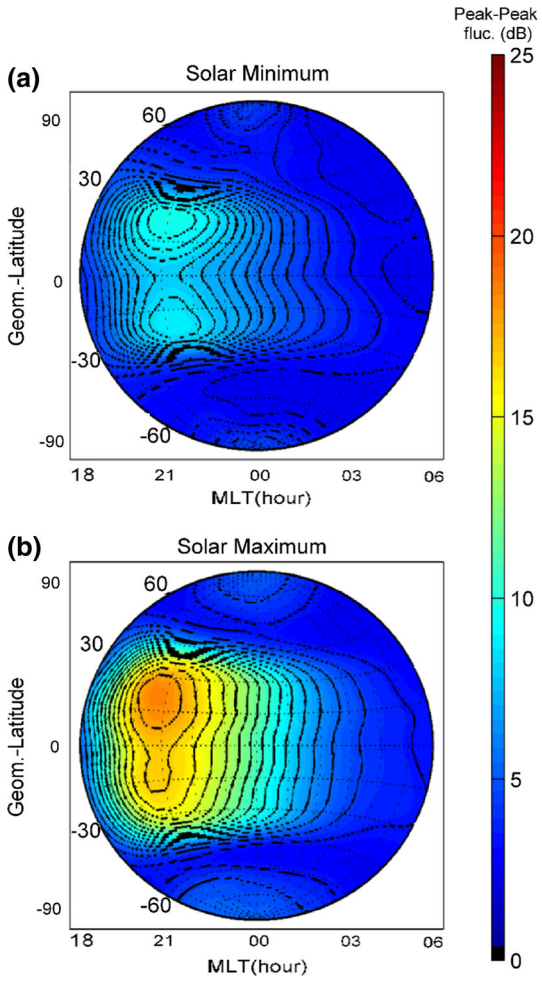

Fig. 4 A gnomonic projection of annual mean diurnal S4max variation for the solar minimum (**a**) and solar maximum (**b**). The vertical integration of S4max is from 50 to 750 km altitude

scintillation starts from 2000 MLT, we then construct the maps by shifting forward 6 h. Figure 4 displays that the low-latitude scintillations situated at ±25° mLat, starting from 2000 MLT, and reaching their maximum intensity at 2100 MLT. The polar-latitude scintillations become prominent at ±60° mLat and develop more strongly toward the magnetic poles but yet with no obvious diurnal variations. Note that, unlike Basu et al. (1988), there is no scintillation zone (intense belt) observed at polar latitudes.

4 Diurnal, Seasonal, and Solar Activity Variations

Figure 3 reveals the seasonal variation of S4max. To study seasonal effects in the F-region in detail, we examine the monthly S4max median at 150–450 km altitude during 2007–2014. The ionosphere F-region has significant geomagnetic control effects. Figure 5 shows that the F-region S4max during 2000–0100 MLT becomes intense and expands over ±30° mLat in the equinox months with relatively higher S4max than during the other

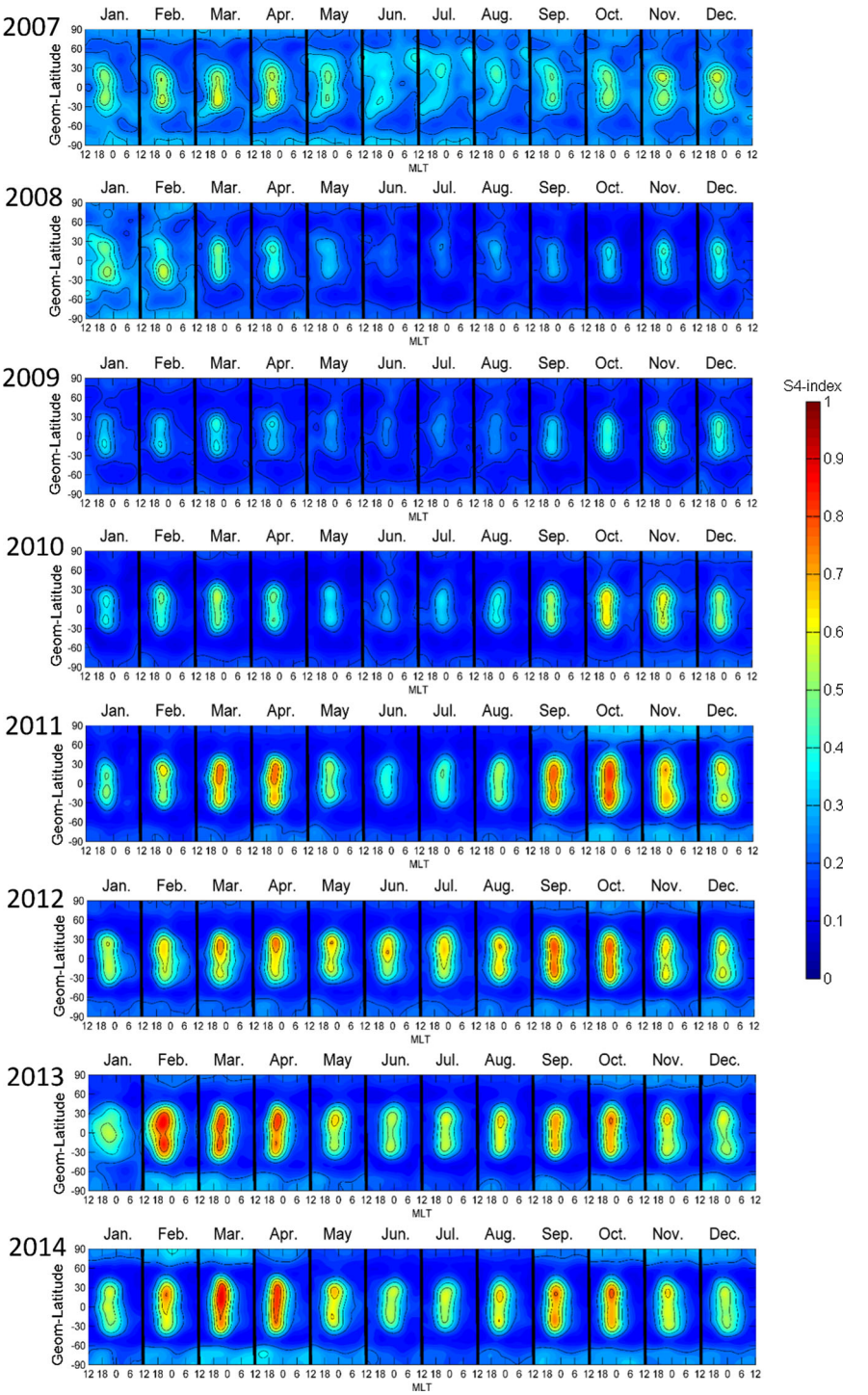

Fig. 5 Illustration of F-region (i.e., 150–450 km) S4max monthly variation in 2007–2014

seasons, and decreases and shrinks down to ±20° in the solstice months. It can be seen that there are fluctuating scintillation patterns appearing in 2007. A detailed study shows these fluctuating patterns result from half of the F3/C constellation (satellite no. 1, no. 3, and no. 4) being at the parking orbit at 500 km altitude and not yet reaching the mission orbit at 800 km in 2007. In general, the intensity and latitudinal range of the F-region S4max are proportional to the solar activity and reach their maximum in the equinox months of the solar maximum 2011 and 2012 (Fig. 5).

On the other hand, the E-region scintillation which is mainly caused by the sporadic-E (Es) layer (Yeh et al. 2014) is significantly affected by the neutral wind, and therefore, its variations will be plotted as a function of the geographic latitude (Fig. 6). Figure 7 reveals that the E-region scintillation, which is the monthly median of the S4max at 80–130 km altitude, appears strongly from 0600 MLT to 2400 MLT, and moves to the middle latitudes in the summer hemisphere. The E-region scintillation has hemispheric asymmetries. For the low- and mid-latitudes, the E-region scintillation in the northern hemisphere during May–August is much more intense than that in the southern hemisphere during November–February. Similarly, in the polar ionosphere, the E-region scintillation, which appears prominently in the nighttime, is more intense in the northern hemisphere than in the southern hemisphere. The overall E-region S4max is greater in 2010–2011 than in 2012–2013 which suggests that the intensity of the E-region scintillation is inversely proportional to the solar activity.

5 Geographic Distribution

Although the diurnal, seasonal, and solar activity variations have been presented, it is essential to know the geographic distribution of the ionospheric scintillations. Figure 7 depicts that the pronounced F-region S4max generally appears along the magnetic equator with a latitudinal zone of ±30°, and the intensity and the altitude in the solar maximum is much greater and higher than those at solar minimum. Although the geographical distribution patterns of pronounced areas for the two solar activities are accordingly similar in each season, the patterns of the four seasons are different in the low latitudes. On the other hand, the E-region S4max prominently centers at 100–110 km altitude and appears in almost all mid-latitudes of 30° to 40° mLat in the northern hemisphere in the J-month and −30° to –40° mLat in the southern hemisphere in the D-month. It is interesting to find that there are lesser intensity zones, for example a gap over North America (−80° to −130° longitude) in J-month and a hole centered over South Africa (−45° to +45° longitude) (Chu et al. 2014). The E-region S4max is much less intense and somewhat symmetric with respect to the magnetic equator in M- and S-months. As expected, the E-region S4max intensity is greater during solar minimum than during solar maximum in all corresponding seasons.

Due to the thickness of the F-region being much larger than that of the E-region, the distributions of the converted (i.e., vertically integrated) S4max are nearly identical to those of the F-region (Fig. 7). Figure 8 further displays the geographical distributions (worst-case maps) of the converted S4max during the solar minimum and maximum conditions. The pronounced pattern generally follows the magnetic equator in the four seasons, taking place from −70° to 0° longitude (South American-Atlantic sector) in D-month, from 0° to 40° and 140° to 210° longitude (African and Pacific sector) in J-month, and around 0° (−60° to 0° in the solar minimum, and −60° to 60° in the solar maximum) longitude (Atlantic sector) in M- and S-month, respectively. In general, the

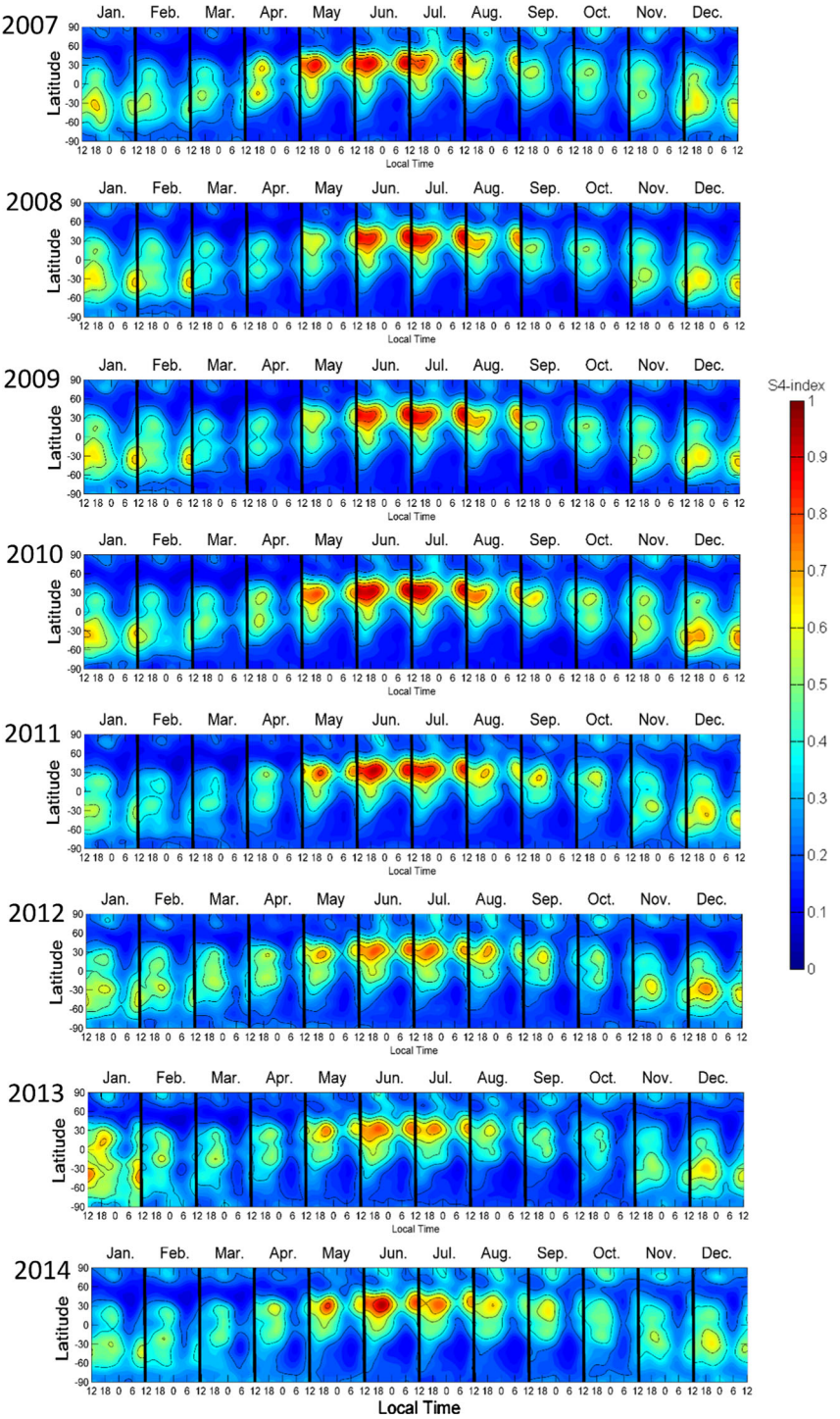

Fig. 6 Illustration of E-region (i.e., 80–130 km) S4max monthly variation in 2007–2014

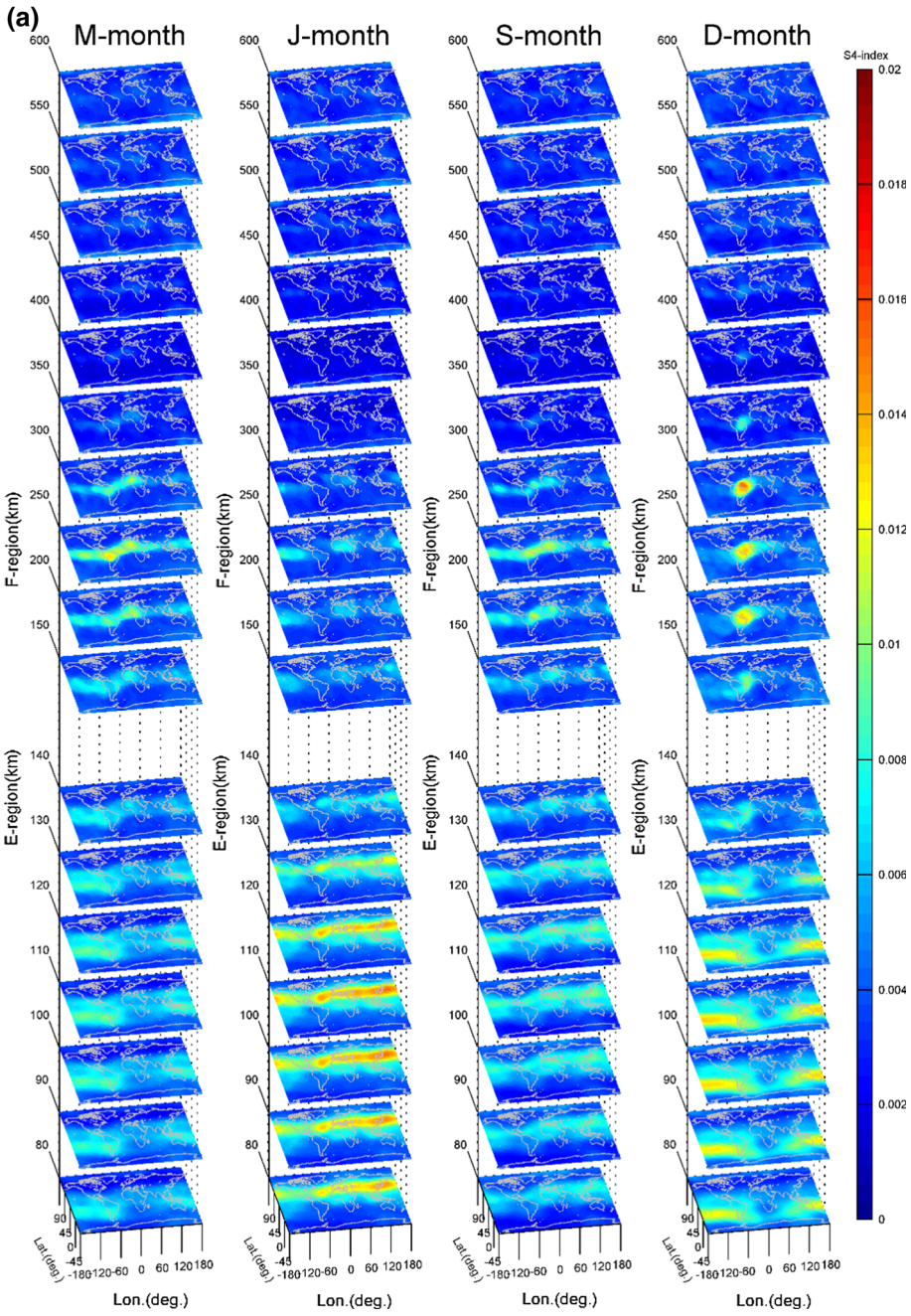

Fig. 7 The distribution of S4max in geographic coordinates for solar minimum (**a**) and solar maximum (**b**). Four columns from left to right stand for M-, J-, S-, and D-months, respectively. The altitude resolution is 10 and 50 km in the E-region (80–150 km) and F-region (150–600 km), respectively

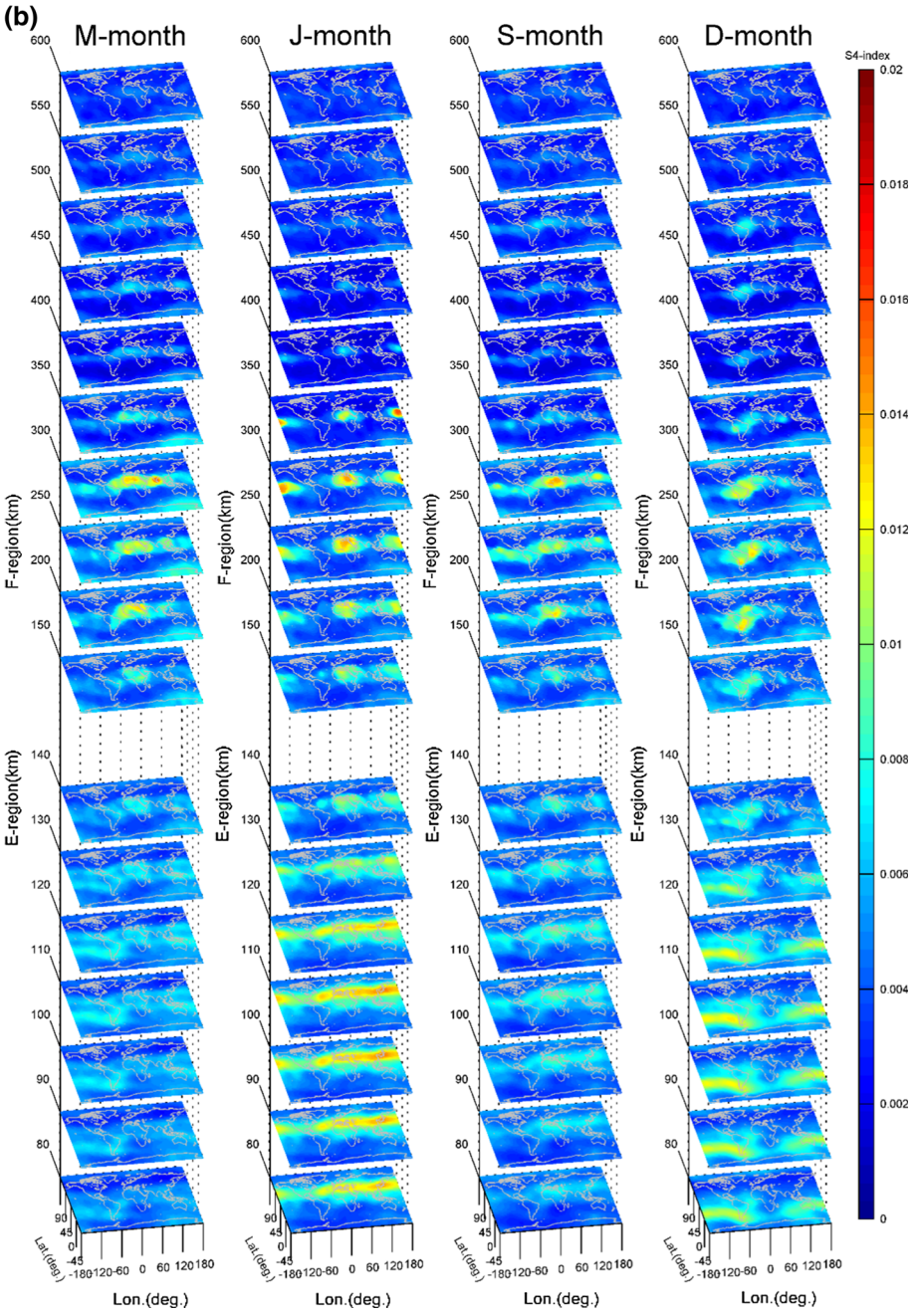

Fig. 7 continued

intense S4max tends to occur between ±30° in magnetic latitude. In the polar latitudes, the F-region S4max is enhanced, and the most pronounced region occurs at longitudes between 90° and 180° in the southern hemisphere during the solar maximum.

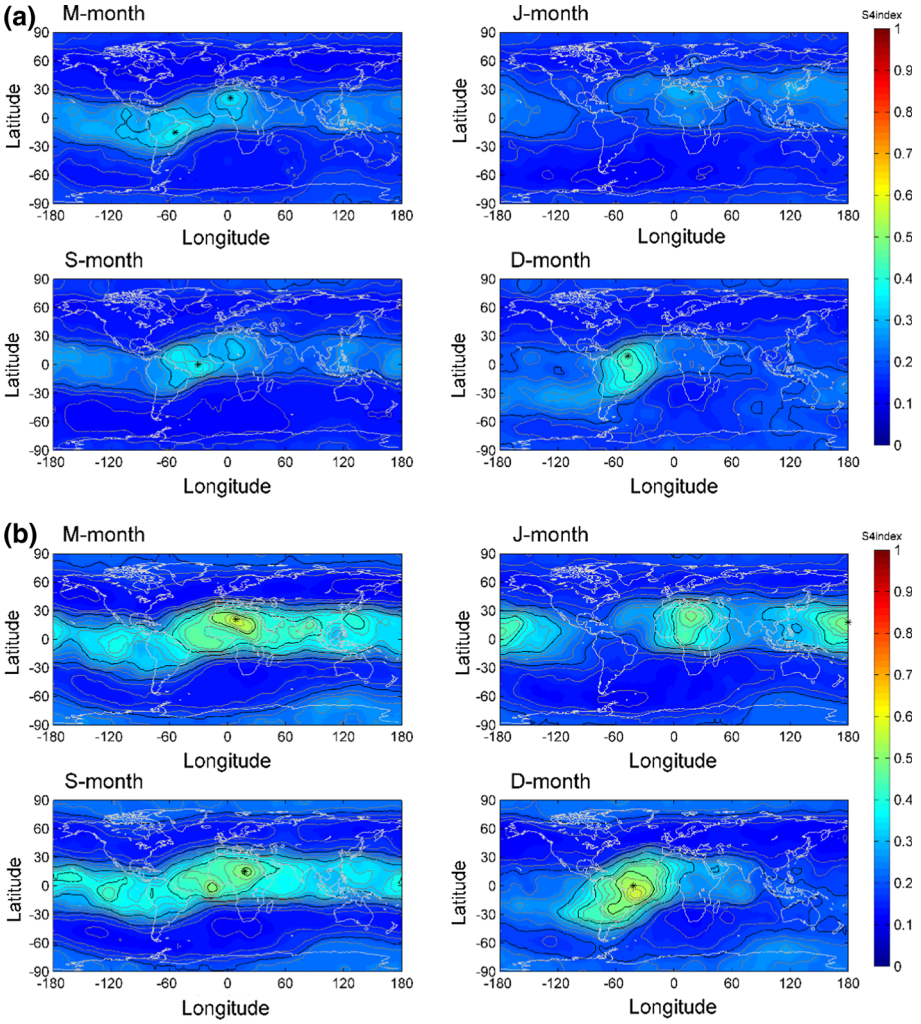

Fig. 8 The altitudinal integration of S4max from 50 to 750 km altitude in the geographical distribution for various seasons in Fig. 7 during the solar minimum (**a**) and solar maximum (**b**)

Based on the similar spirit of Basu et al. (1988), we construct the worst-case map using geographical coordinates during the solar minimum and maximum. Figure 9 illustrates that, at low latitudes, the most intense scintillations occur in the South American-African sector centering over the South American region in the solar minimum, while centering over the African region for the solar maximum, and the scintillation in the solar maximum is much greater than that in the solar minimum. It can be seen that the weakest low-latitude scintillations appear between 70° and 90° and between −80° and −100° in the solar minimum. On the other hand, the polar latitude scintillation is greater in the solar maximum than that in the solar minimum and yields its greatest value at longitude 90°–130°, and 60°–200°, in the southern hemisphere during solar minimum and solar maximum, respectively.

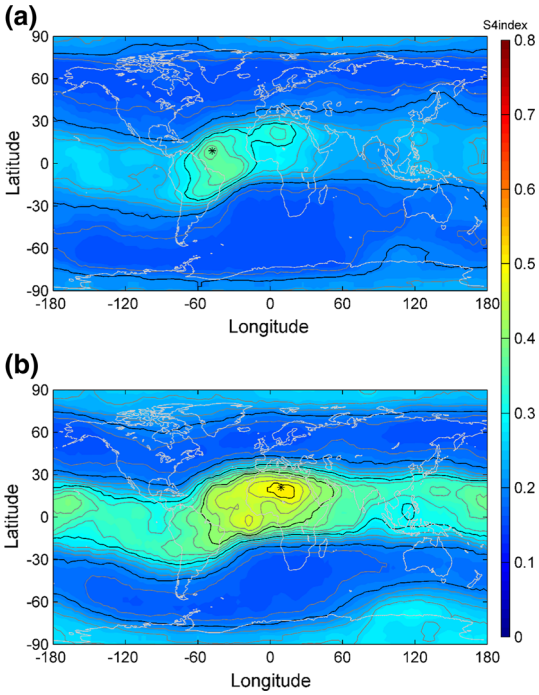

Fig. 9 The altitudinal integration of S4max geographical distribution during the solar minimum (**a**) and solar maximum (**b**). The vertical integration of S4max is from 50 to 750 km altitude

6 Discussion and Conclusions

Basu et al. (1988) constructed worst-case scintillation maps which showed that the low-latitude S4 scintillation locates at ±20° mLat, starts around 2000 MLT, and ends by about midnight in both the solar maximum and minimum. Their results reveal that a double-peaked "feather" shape appears in the solar maximum, while a single peak occurs in the solar minimum. The high latitude S4 scintillation appears above 60° mLat. To cross compare our results with those of Basu et al. (1988), we construct similar figures but from 1800 to 0600 MLT. Figure 4 shows that the low-latitude-converted S4maxs are located at ±30°, centering at around ±20° mLat, appear at 1900 MLT, reach their maximum at 2100 MLT, and vanish by about 0200–0300 MLT. In equatorial/low latitudes, our results shown in Fig. 4 and the results published in Basu et al. (1988) are generally similar, except that we observe the double-peaked features in both solar minimum and maximum. Meanwhile, at polar latitudes, the scintillation intensity of our S4max study is proportional to the latitude (for detail, see Fig. 3), while that of the L-band scintillations of Basu et al. (1988) yields the intense zone (belt). Generally, the scintillation intensity of this study is much weaker than that of Basu et al. (1988).

Su et al. (2006) observed the global distribution of the occurrence rate for ion density irregularities at 600 km in the topside ionosphere by using the data of the ROCSAT-1 satellite during moderate-to-high solar activity years of 1999–2004. They found that the density irregularity is most frequently observed in longitudes between 0° to 60° (African sector) in the June solstice, March and September equinoxes, and shifts to longitudes between −60° to 0° (Atlantic sector) during the December solstice. In the June solstice, a second high occurrence rate appears in longitudes between 150° to 210° (Pacific sector).

The geographic distribution of F-region S4max is nearly identical to those of the occurrence rate for density irregularities reported by Su et al. (2006). It can be seen that the geographic distribution of the E-region S4max is very different from that of the F-region S4max.

Figures 2 and 6 show that the E-region S4max reach their maximum values in the summer hemisphere (northern hemisphere in J-month and southern hemisphere in D-month). These maximum phenomena are due to the two mechanisms of sporadic-E (Es) layer formation, the meteor ionization mechanism and wind shear theory, which are the contributor of ionized particles and the environment of the sporadic-E (Es) layer formation, respectively (Yeh et al. 2014). The observations show that the meteor numbers in J- and D-months are much larger than in M- and S-months. Therefore, the meteor tails provide many more ionized particles to form larger irregularity intensities in J- and D-months than in M- and S-months (Yeh et al. 2014). Meanwhile, the hemisphere difference in J- and D-months is due to the convergence mechanism caused by the negative vertical gradient of the horizontal wind velocity, which occurs mainly in the summer hemisphere (Yeh et al. 2012, 2014). Figures 2 and 5 show that the nighttime F-region irregularities become intense, reach greater altitudes, and move to higher latitudes in the equinox M- and S-months and the solar maximum. These might result from that the **ExB** plasma fountain due to the pre-reversal enhancement which increases in the equinoxes and at solar maximum (Kelley 2009).

It can be seen that the geographic distributions of the converted S4max in the four seasons shown in Fig. 8 are slightly different from those of Su et al. (2006). Sun et al. (2015) examine the intensity of low-latitude nighttime F-region ionospheric density irregularities observed by ROCSAT-1 and ground-based GPS receivers in solar maximum. They suggest that differences between the two observations might result from ROCSAT-1 probing ionospheric irregularities at its 600 km orbital altitude and, however, a ground-based station simultaneously detecting all the irregularities along the slant path from the GPS satellite to the receiver. Therefore, the slight pattern discrepancy between Fig. 8b and Su et al. (2006) might occur because the converted S4max is computed by integrating S4max instead of RO S4 index from 50 km altitude to the satellite altitude in this study, while the occurrence rate is derived from in situ measurements of ion density at a satellite height of about 600 km altitude by Su et al. (2006).

We validate the converted S4max by cross comparing it with the ground-based GPS scintillation at 10°–25°S, 100°–130°E recorded by the Bureau of Meteorology, Australia (http://www.ips.gov.au/). Figure 10 shows that the two observations yield similar tendencies in diurnal, seasonal, and solar activity variations, except for the F3/C S4max being constantly greater than the ground-based S4 index. The discrepancy might result from the fact that the scintillation is derived from the greatest value of F3/C S4, while the ground-based one is computed as its median value.

In summary, F3/C provides a global uniform 3D structure of L-band scintillation observations. The converted S4max can be used for understanding the appearance time and the geographic distribution of ionospheric scintillations, which will benefit practical uses for communication, navigation, and positioning applications on the ground. In fact, the 3D structure of the F3/C S4 scintillation observations should benefit the satellite–satellite link of communication, navigation, and positioning. The worst-case scintillation on the ground appears in the low latitude of ±30°, peaking at around ±20° mLat from the post-sunset of 1900 MLT till post-midnight of 0200–0300 MLT. The region which experiences the worst-case scintillations is the low-latitude ionosphere between South America and Africa.

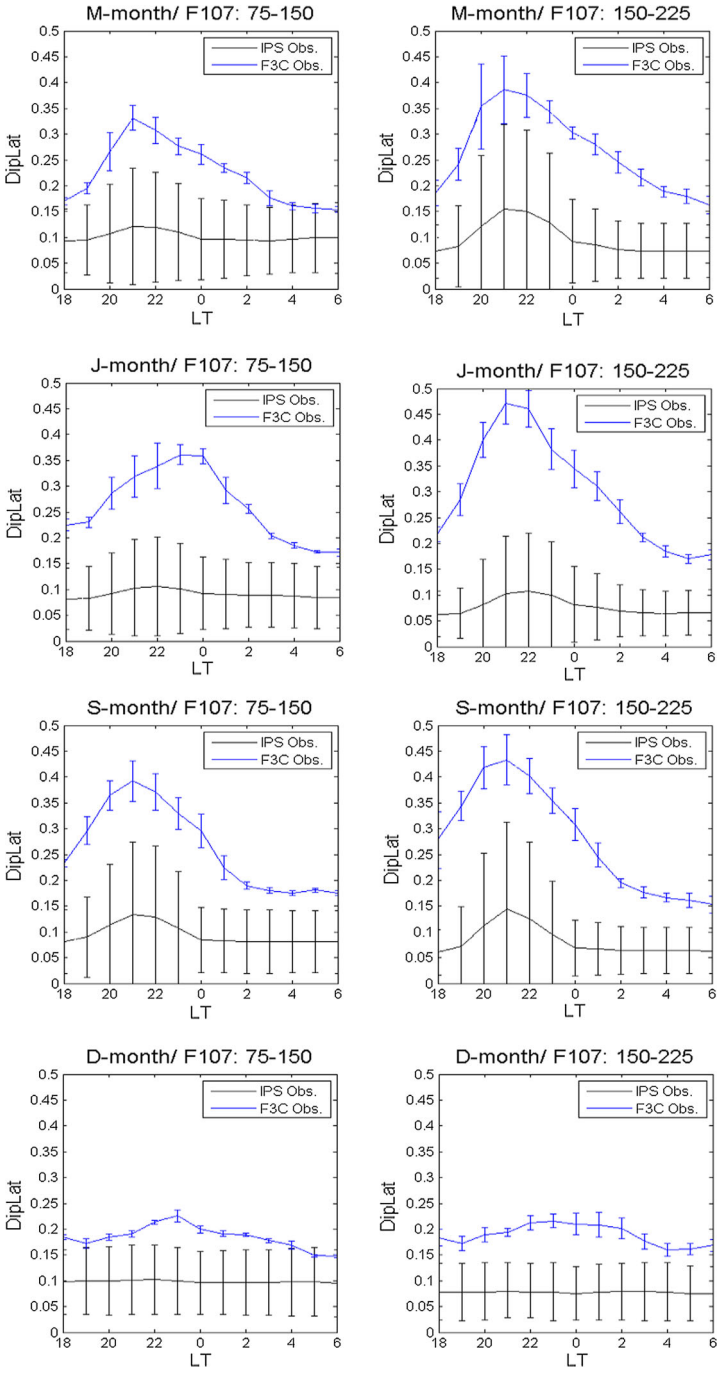

Fig. 10 A cross comparison between F3/C S4max and ground-based S4 index observations for solar minimum (*left panel*) and solar maximum (*right panel*)

Acknowledgments The authors thank Prof. Chao-Han Liu at Academia Sinica for useful comments and suggestions. The F3/C S4max data are retrieved from the COSMIC Data Analysis and Archival Center (CDAAC) and the Taiwan Analysis Center for COSMIC (TACC). Taiwan. This study has been partially supported by the project, MOST 103-2628-M-008-001, granted by Ministry of Science and Technology (MOST) to National Central University. The authors thank the Editor in Chief for his suggestions for editorial improvements.

References

Aarons J, Klobuchar JA, Whitney HE, Austen J, Johnson AL, Rino CL (1983) Gigahertz scintillations associated with equatorial patches. Radio Sci 18(3):421–434

Aarons J, Mendillo M, Yantosca R (1997) GPS phase fluctuations in the equatorial region during sunspot minimum. Radio Sci 32(4):1535–1550

Abdu MA (2001) Outstanding problems in the equatorial ionosphere thermosphere electrodynamics relevant to spread-F. J Atmos Solar Terr Phys 63:869–884

Anthes RA, Ector D, Hunt DC, Kuo Y, Rocken C, Schreiner WS, Sokolovskiy SV, Syndergaard S, Wee T, Zeng Z, Bernhardt PA, Dymond KF, Chen Y, Liu H, Manning K, Randel WJ, Trenberth KE, Cucurull L, Healy SB, Ho S, McCormick C, Meehan TK, Thompson DC, Yen NL (2008) The COSMIC/FORMOSAT-3 mission: early results. Bull Am Met Soc 89:313–333

Arras C, Wickert J, Beyerle G, Heise S, Schmidt T, Jacobi C (2008) A global climatology of ionospheric irregularities derived from GPS radio occultation. Geophys Res Lett 35:L14809. doi:10.1029/2008GL034158

Azpilicueta F, Brunini C, Radicella SM (2006) Global ionospheric maps from GPS observations using modip latitude. Adv Space Res 38(11):2324–2331

Basu S, MacKenzie E, Basu S (1988) Ionospheric constraints on VHF = UHF communication links during solar maximum and minimum periods. Radio Sci 23:363

Brahmanandam PS, Uma G, Liu JY, Chu YH, Latha Devi NSMP, Kakinami Y (2012) Global S4 index variations observed using FORMOSAT-3/COSMIC GPS RO technique during a solar minimum year. J Geophys Res 117:A09322. doi:10.1029/2012JA017966

Burke WJ, Gentile LC, Huang CY, Valladares CE, Su SY (2004) Longitudinal variability of equatorial plasma bubbles observed by DMSP and ROCSAT-1. J Geophys Res 109:A12301. doi:10.1029/2004JA010583

Chu YH, Wang CY, Wu KH, Chen KT, Tzeng KJ, Su CL, Feng W, Plane JMC (2014) Morphology of sporadic E layer retrieved from COSMIC GPS radio occultation measurements: wind shear theory examination. J Geophys Res Space Phys 119:2117–2136. doi:10.1002/2013JA019437

Frihagen J, Troim J (1960) Scintillation of the 20 Mc/s signal from the earth satellite 1958δII. J Atmos Terr Phys 18:75–78

Hocke K, Pavelyev A, Yakovlev O, Barthes L, Jakowski N (1999) Radio occultation data analysis by radio holographic method. J Atmos Solar-Terr Phys 61:1169–1177

Hook JL, Owren L (1962) The vertical distribution of E-region irregularities deduced from scintillations of satellite radio signals. J Geophys Res 67(13):5353–5357

Huang CY, Burke WH, Machuzak JS, Gentile LC, Sultan PJ (2002) Equatorial plasma bubbles observed by DMSP satellites during a full solar cycle: toward a global climatology. J Geophys Res 107(A12):1434. doi:10.1029/2002JA009452

Kelley MC (2009) The earth's ionosphere: plasma physics and electrodynamics, 2nd edn. Academic, San Diego

Mendillo M, Lin B, Aarons J (2000) The application of GPS observations to equatorial aeronomy. Radio Sci 35(3):885–904. doi:10.1029/1999RS002208

Olwendo O (2013) Studies in ionospheric TEC and equatorial scintillation over Kenyan region using GPS receivers, ionospheric monitoring: Africa Workshop, Hermanus, South Africa, 24–25 January 2013

Parthasarathy R, Reid GC (1959) Signal strength recordings of the satellite 1958δ2 (Sputnik III) at College Alaska. Proc IRE 47:78–79

Rastogi RG (1980) Seasonal variation of equatorial spread-F in the American and Indian zones. J Geophys Res 85(2):722–726

Rino C (2011) The theory of scintillation with applications in remote sensing. Wiley-IEEE Press, Hoboken

Sahai Y, Fagundes PR, Bittencourt JA (2000) Transequatorial F-region ionospheric plasma bubbles: solar cycle effects. J Atmos Sol-Terr Phys 62:1377–1383

Scherliess L, Fejer BG (1999) Radar and satellite global equatorial F region vertical drift model. J Geophys Res 104:6829–6842. doi:10.1029/1999JA900025

Sokolovskiy S, Schreiner W, Rocken C, Hunt D (2002) Detection of high-altitude ionospheric irregularities with GPS/MET. Geophys Res Lett 29:3. doi:10.1029/2001GL013398

Straus PR, Anderson PC, Danaher JE (2003) GPS occultation sensor observations of ionospheric scintillation. Geophys Res Lett 30(8):1436. doi:10.1029/2002GL016503

Su SY, Liu CH, Ho HH, Chao CK (2006) Distribution characteristics of topside ionospheric density irregularities: equatorial versus midlatitude region. J Geophys Res 111:A06305. doi:10.1029/2005JA011330

Sun YY, Liu JY, Chao CK, Chen CH (2015) Intensity of low-latitude nighttime F-region ionospheric density irregularities observed by ROCSAT and ground-based GPS receivers in solar maximum. J Atmos Solar-Terr Phys 123:92–101. doi:10.1016/j.jastp.2014.12.013

Thampi SV, Yamamoto M, Tsunoda RT, Otsuka Y, Tsugawa T, Uemoto J, Ishii M (2009) First observations of large-scale wave structure and equatorial spread-F using CERTO radio beacon on the C/NOFS satellite. Geophys Res Lett 36:L18111. doi:10.1029/2009GL039887

Thébault E, Finlay CC, Beggan CD, Alken P, Aubert J, Barrois O, Bertrand F, Bondar T, Boness A, Brocco L, Canet E, Chambodut A, Chulliat A, Coïsson P, Civet F, Du A, Fournier A, Fratter I, Gillet N, Hamilton B, Hamoudi M, Hulot G, Jager T, Korte M, Kuang W, Lalanne X, Langlais B, Jean- Léger M, Lesur V, Lowes FJ, Macmillan S, Mandea M, Manoj C, Maus S, Olsen N, Petrov V, Ridley V, Rother M, Sabaka TJ, Saturnino D, Schachtschneider R, Sirol O, Tangborn A, Thomson A, Tøffner-Clausen L, Vigneron P, Wardinski I, Zvereva T (2015) International geomagnetic reference field: the 12th generation. Earth Planets Space 67:79. doi:10.1186/s40623-015-0228-9

Uma G, Liu JY, Chen SP, Sun YY, Brahmanandam PS, Lin CH (2012) A comparison of the equatorial spread F derived by the International Reference Ionosphere and the S4 index observed by FORMOSAT-3/COSMIC during the solar minimum period of 2007–2009. Earth Planets Space 64:467–471

Watanabe S, Oya H (1986) Occurrence characteristics of low latitude ionosphere irregularities observed by impedance probe on board the Hinotori satellite. J Geophys Res 38:125–149

Wickert J et al (2001) Atmosphere sounding by GPS radio occultation: first results from CHAMP. Geophys Res Lett 28(17):3263–3266

Wu DL, Ao CO, Hajj GA et al (2005) Sporadic E morphology from GPS-CHAMP radio occultation. J Geophys Res 110:A01306. doi:10.1029/2004JA010701

Wu DL et al (2006) Remote sounding of atmospheric gravity waves with satellite limb and nadir techniques. Adv Space Res 37:2269–2277

Yeh WH, Huang CY, Hsiao TY, Chiu TC, Lin CH, Liou YA (2012) Amplitude morphology of GPS radio occultation data for sporadic-E layers. J Geophys Res 117:A11304. doi:10.1029/2012JA017875

Yeh WH, Liu JY, Huang CY, Chen SP (2014) Explanation of the sporadic-E layer formation by comparing FORMOSAT-3/COSMIC data with meteor and wind shear information. J Geophys Res Atmos 119:4568–4579. doi:10.1002/2013JD020798

Yunck T, Liu CH, Ware R (2000) A history of GPS sounding. Terr Atmos Oceanic Sci 11:1–20